







# Targeted Electrocatalysis for High-Performance Lithium–Sulfur Batteries


Aqsa Nazir , Anil Pathak , Dambar Hamal, Osama Awadallah , Saeme Motevalian , Ana Claus , Vadym Drozd, and Bilal El-Zahab\* 

**The intricate sulfur redox chemistry involves multiple electron transfers and complicated phase changes. Catalysts have been previously explored to overcome the kinetic barrier in lithium–sulfur batteries (LSBs). This work contributes to closing the knowledge gap and examines electrocatalysis for enhancing LSB kinetics. With a strong chemical affinity for polysulfides, the electrocatalyst enables efficient adsorption and accelerated electron transfer reactions. Resulting cells with catalyzed cathodes exhibit improved rate capability and excellent stability over 500 cycles with 91.9% capacity retention at C/3. In addition, cells were shown to perform at high rates up to 2C and at high sulfur loadings up to 6 mg cm<sup>−2</sup>. Various electrochemical, spectroscopic, and microscopic analyses provide insights into the mechanism for retaining high activity, coulombic efficiency, and capacity. This work delves into crucial processes identifying pivotal reaction steps during the cycling process at commercially relevant areal capacities and rates.**

## 1. Introduction

Lithium–sulfur batteries (LSBs) represent an exciting chemistry in the pursuit of new rechargeable energy storage solutions. Recognized for their high energy density and cost-effectiveness,<sup>[1–4]</sup> LSBs hold great promise for powering the next generation of electronic devices and electric vehicles. Nonetheless, the path toward optimizing their efficiency, durability, and environmental sustainability is riddled with complex electrochemical challenges, most notably the complex dynamics inherent to polysulfides during the charge and discharge processes.<sup>[5,6]</sup> The promise of LSBs relies on their ability to harness the sulfur to sulfide chemistry, a process governed by a sequence of intricate redox reactions. These reactions include the reversible conversion of elemental sulfur in the form of octosulfur (S<sub>8</sub>) into soluble lithium polysulfides (LiPS) and eventually into lithium sulfide during discharge, followed by their reconversion to S<sub>8</sub> during the charge. This sulfur redox chemistry forms the bedrock of energy storage in LSBs, yet it poses numerous challenges, prominently concerning the dissolution and migration of LiPS, that can lead to capacity decay and diminished cycle life.

Dr. A. Nazir, Dr. A. Pathak, Dr. D. Hamal, Dr. O. Awadallah, S. Motevalian, A. Claus, Dr. V. Drozd, Prof. B. El-Zahab  
Department of Mechanical and Materials Engineering, College of Engineering and Computing, Florida International University, Miami, FL 33174, USA  
E-mail: belzahab@fiu.edu

 The ORCID identification number(s) for the author(s) of this article can be found under <https://doi.org/10.1002/eem2.12844>.

DOI: 10.1002/eem2.12844

LiPS loss from the cathode driven by the concentration gradient and its contribution to low coulombic efficiency represents one of the most frequently reported challenges limiting LSBs.<sup>[6–9]</sup> This problem originates during the formation of polysulfides. As these soluble polysulfides detach from the sulfur host, they become susceptible to diffusion from the cathode into the electrolyte during cell operation. As the polysulfides reach the anode surface, they participate in parasitic reactions that lead to poor coulombic efficiency and irreversible consumption of active lithium and sulfur.<sup>[10]</sup> Numerous research efforts have focused on restraining the shuttle mechanism to improve coulombic efficiency and cyclability.<sup>[11–14]</sup> A prevalent strategy has been the physical confinement of polysulfides using porous host materials including single-atom iron sites in

N-doped porous carbon on CNTs<sup>[15]</sup> and hollow carbonaceous nanovessel fibers with atomically dispersed CoN<sub>4</sub> electrocatalysts.<sup>[16]</sup> However, physical confinement introduces constraints on mass transport and sulfur loading. Further work is still needed to develop optimal solutions that can effectively suppress polysulfide migration while maintaining the high energy density promised by the Li–S chemistry. New insights into the underlying chemical interactions governing polysulfide solubility may enable more effective shuttle inhibition through rational design of the cathode/electrolyte interface.

The sluggish kinetics of LSBs, particularly under lean electrolyte conditions, have been universally observed and are generally accepted as intrinsic to the complex sulfur redox chemistry.<sup>[17–20]</sup> This presents a major obstacle for practical LSBs, as the electrochemical conversion reactions from soluble polysulfide intermediates to solid discharge products such as Li<sub>2</sub>S<sub>2</sub>/Li<sub>2</sub>S inherently have a large overpotential causing major energy efficiency losses and limit the battery's rate capability.<sup>[21]</sup> Recent studies have instead pointed to kinetic problems experienced in the cells during the sulfur reduction reaction that exacerbate the shuttle effect.<sup>[22,23]</sup> Overcoming the intrinsically slow conversion kinetics is therefore critical for enabling high-performance LSBs. LSBs often suffer from poor rate capability and cycle life that have been attributed to three main phenomena: 1) passivating 2D depositions of solid sulfides, 2) sluggish kinetics, and 3) poor coulombic efficiency. These issues are graphically summarized in **Figure 1**.

To overcome these challenges, the LSB community has increasingly focused on developing efficacious electrocatalysts.<sup>[24]</sup> Carbon materials such as nanotubes and mesoporous carbon can physically

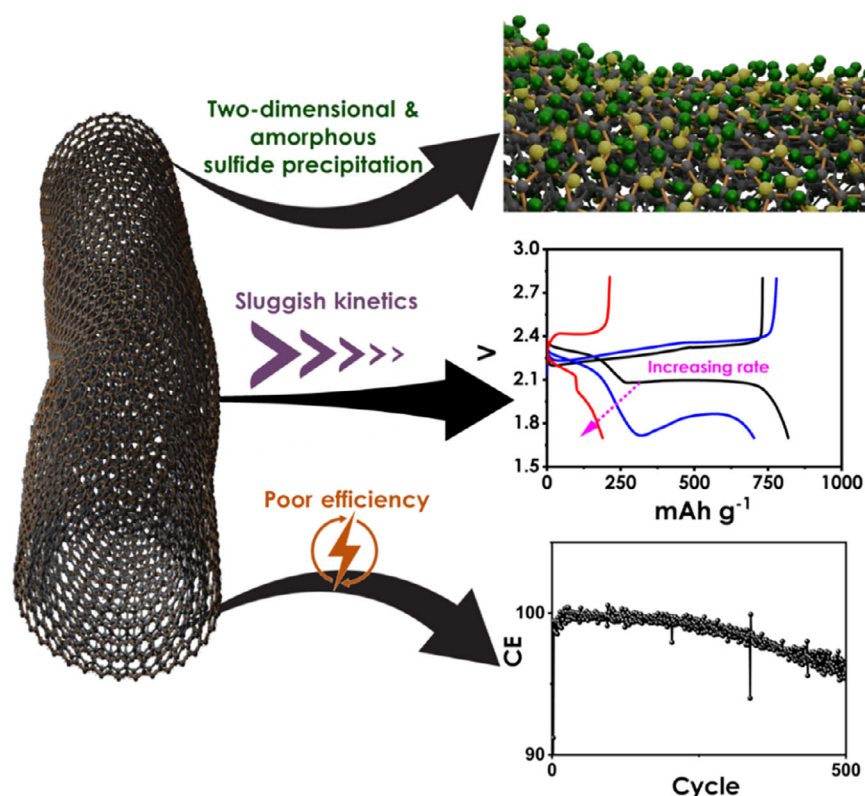


**Figure 1.** Schematic illustration of the major issues facing LSBs with carbon-based cathodes that include two-dimensional and amorphous sulfide precipitation, sluggish kinetics, and poor coulombic efficiency (CE).

accommodate (nonpolar nature) sulfur but cannot sufficiently suppress the shuttle mechanism for stable cycling. Using catalysts can promote polysulfide adsorption and redox reactions to enhance performance. Various catalyst materials like metal sulfides, nitrides, and phosphides have demonstrated the ability to chemically bind polysulfides while lowering kinetic barriers and enabling uniform  $\text{Li}_2\text{S}$  product formation.<sup>[5,21,22,25–27]</sup> This helps mitigate issues with the shuttle mechanism and suboptimal reaction kinetics. For instance, bismuth sulfide was shown to provide the maximum p-electron gain to sulfur, reducing the activation barrier for insoluble polysulfide deposition.<sup>[25]</sup> Similarly, cobalt diselenide offered abundant adsorption sites to retain polysulfides and accelerate conversion reactions.<sup>[28]</sup> Related studies on chromium nitride composites demonstrated a promoted polysulfide conversion and 3D  $\text{Li}_2\text{S}$  growth that enhanced cathode kinetics.<sup>[29]</sup> However, few notable efforts have been carried out to shed a light on polysulfide adsorption and its correlation to reaction kinetics. For example, Zhang et al.<sup>[30]</sup> discussed, optimizing the adsorption-catalysis-desorption balance could be key, rather than simply maximizing adsorption capacity. Still, questions remain regarding polysulfide adsorption, solid discharge products formation and its correlation to reaction kinetics, for example, sustaining catalysis after the catalyst surfaces are covered by solid discharge products (including, leftover solid discharge products that formed during previous cycles) poses an unresolved challenge. Kung et al.<sup>[31,32]</sup> showcased the effectiveness of iron and tin plating in enhancing sulfur utilization and battery performance. These studies collectively highlight the potential of metal-based catalysts and coatings, including Pt, in addressing key

challenges in Li-S battery technology. Shang et al. developed a hybrid composite of nitrogen-doped carbon-wrapped bimetallic cobalt-iron alloy nanoparticles ( $\text{NC@CoFe}$ ), which demonstrated strong polysulfide anchoring and catalytic conversion capabilities when used as a separator coating in Li-S batteries.<sup>[33]</sup>

While most LSB using electrocatalysts do provide improved LSB performance, they often experience a steady decline over the course of cycling partly due to the instability of the metal catalyst. Instead, oxides, sulfides, and selenides can provide the improved stability, but they suffer from low conductivity that could negatively impact the LSB's rate performance. In this work, platinum (Pt) was selected as a model system since it is a well-studied electrocatalyst both alone and as an alloy. Pt is both stable and highly active under a wide range of battery operating conditions of electrolyte, voltage window, and passivating conditions. In addition, Pt, notwithstanding its relatively minute proportion—typically constituting less than 0.02% of the weight of the battery—has been shown to significantly boost key reactions as has been previously reported.<sup>[26,34–36]</sup> Han et al. have also shown that Pt has the ability to catalyze the redox reactions of LSB bidirectionally, synergistically enhancing the catalytic effect and reaction kinetics of sulfur species of  $\text{LiPS}$ .<sup>[36,37]</sup>

Herein, we investigate the electrocatalysis impact of Pt nanocatalysts supported on carbon nanotubes on the sulfur reduction reaction (SRR) in LSB studies. The Pt-CNT composites with dispersed Pt nanoparticles provide  $\text{LiPS}$  binding sites, improved kinetics of conversion, and suitable nucleation sites for the deposition of the discharge species. As a proof-of-concept study, this work highlights thorough theoretical calculation, electrochemical tests, and analytical methods to help elucidate the mechanism these catalysts have on the efficiency, reversibility, rate capability, and long-term stability of LSB with commercially relevant loadings and current densities.

## 2. Computational Section

Computational modeling using density functional theory (DFT) was carried out with the Vienna *ab initio* simulation package (VASP), version 6.3.<sup>[38,39]</sup> To account for exchange and correlation effects, we employed the Perdew–Burke–Ernzerhof (PBE) formulation of the generalized gradient approximation (GGA)<sup>[40]</sup> The electron wave functions were represented by plane waves, with an energy cutoff set at 520 eV. Dispersion interactions were included using the D3 method developed by Grimme.<sup>[41]</sup> The supercell for the graphene-based surfaces includes 72 carbon atoms. Graphene surfaces were separated from each other by 25 Å vacuum layers. Monkhorst-Pack<sup>[42]</sup> k-point grids were set as  $5 \times 5 \times 1$ . Atomic relaxation was performed until the change in the electronic and ionic steps were less than  $10^{-5}$  and  $10^{-4}$  eV, respectively. Molecular species were placed above several possible adsorption

sites on the graphene surface. For each system, the one leading to the lowest total energy of the system was chosen for further calculations and analysis.

The adsorption energies of  $\text{Li}_2\text{S}_x$  on the graphene were calculated using formulas:

$$E_{\text{ads}} = E_{\text{S-Li}_2\text{S}_n} - E_{\text{S}} - E_{\text{Li}_2\text{S}_n}, \quad (1)$$

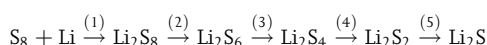
where  $E_{\text{S-Li}_2\text{S}_n}$ ,  $E_{\text{S}}$ , and  $E_{\text{Li}_2\text{S}_n}$  are DFT total energies of  $\text{Li}_2\text{S}_x$  ( $n = 2, 4, 6, 8$ ) adsorbed on the graphene, graphene substrate, and isolated molecules, respectively.

The charge density difference was calculated according to the expression:

$$\rho = \rho_{\text{adsorbed state}} - (\rho_{\text{adsorbate}} + \rho_{\text{graphene}}), \quad (2)$$

where  $\rho_{\text{adsorbed state}}$ ,  $\rho_{\text{adsorbate}}$ , and  $\rho_{\text{graphene}}$  are charge transfer of  $\text{Li}_2\text{S}_x$  adsorbed on the graphene, isolated  $\text{Li}_2\text{S}_x$ , and graphene with or without Pt, respectively. The VESTA software<sup>[43]</sup> was used for atomic visualization and charge density differences calculations.

The following reactions were taken into consideration for the discharge process:



The corresponding relative free energies of these reactions on the pristine and Pt-modified graphene were obtained using Equations (3)–(7), respectively:

$$E_{\text{S-Li}_2\text{S}_8} - E_{\text{S}_8} + 2E_{\text{Li}} \quad (3)$$

$$E_{\text{S-Li}_2\text{S}_6} + \frac{1}{4}E_{\text{S}_8} - E_{\text{S-Li}_2\text{S}_8} \quad (4)$$

$$E_{\text{S-Li}_2\text{S}_4} + \frac{1}{4}E_{\text{S}_8} - E_{\text{S-Li}_2\text{S}_6} \quad (5)$$

$$E_{\text{S-Li}_2\text{S}_2} + \frac{1}{4}E_{\text{S}_8} - E_{\text{S-Li}_2\text{S}_4} \quad (6)$$

$$E_{\text{S-Li}_2\text{S}} + \frac{1}{8}E_{\text{S}_8} - E_{\text{S-Li}_2\text{S}_2} \quad (7)$$

where  $E_{\text{Li}}$  is total energy of Li atom and  $E_{\text{S}_8}$  is total energy of  $\text{S}_8$  molecule in the vacuum,  $E_{\text{S-Li}_2\text{S}_n}$  is the total energy of adsorbed  $\text{Li}_2\text{S}_x$  molecules.

Optimized geometrical configurations (side and top views) of  $\text{Li}_2\text{S}_x$  adsorbed on the pristine, graphene, and Pt@Gr are shown below. Platinum adatom was found to occupy a bridge adsorption site between two carbon atoms on the graphene sheet. This result agrees with Manade et al.<sup>[44]</sup> who found a bridge adsorption site as a preferable one for Pt adatom on the graphene surface.

### 3. Results and Discussion

The performance of lithium–sulfur coin cells employing a sulfur-composite cathode was first evaluated. The cathode was composed of 64% sulfur (Figure S4, Supporting Information) with a relatively lean

electrolyte-to-sulfur (E/S) ratio of 6  $\mu\text{L}/\text{mg}$ , representing the type of practical conditions often studied in coin cell-based LSBs. The sulfur loading used in this work ranged from 1.65 to 6  $\text{mg cm}^{-2}$ , while most of the electrochemical studies were conducted for 3–4  $\text{mg cm}^{-2}$ , a value approaching what may be commercially expected. The cells were tested under varied current densities of 0.167, 0.335, and 0.558  $\text{A g}^{-1}$  based on sulfur loading. Additionally, a current density of 1.67  $\text{mA cm}^{-2}$  (0.558  $\text{A g}^{-1}$ ) was chosen for the cycling experiments as it models values generally reported for Li-ion batteries. Assessing the performance under these lean-electrolyte and moderate-loading conditions provides insight into the pragmatic viability of the cathode system.

In a typical LSB battery, the galvanostatic voltage profile shows significant variation in the second discharge plateau arising during the conversion of higher order polysulfides (mainly  $\text{Li}_2\text{S}_4$ ) to insoluble  $\text{Li}_2\text{S}_2$  and  $\text{Li}_2\text{S}$  (Figure S6, Supporting Information). At the lower current density of 0.167  $\text{A g}^{-1}$ , the discharge profile shows the key expected features, an initial sloping region corresponding to the dissolution of cyclo- $\text{S}_8$ , followed by a high voltage plateau from 2.35 to 2.25 V where predominantly longer chain polysulfides are formed, and finally a second plateau at 2.1 V representing the reduction of  $\text{Li}_2\text{S}_4$  to  $\text{Li}_2\text{S}_2/\text{Li}_2\text{S}$ .<sup>[7]</sup> A small voltage dip is observable at the onset of this low voltage plateau, indicative of the potential barrier for solid product nucleation.<sup>[45,46]</sup> However, increasing the specific current to 0.558  $\text{A g}^{-1}$  results in an intense deepening of this discharge voltage dip, reaching as low as 1.8 V before recovering to 2.0 V. In contrast, the charge voltage profile obtained at the same rate exhibits no such drastic overpotential at any given time. This implies that the discharge potential barrier does not stem from mass transport effects, but instead points to sluggish reaction kinetics for the conversion of dissolved polysulfides to solid sulfides. Specifically, the precipitation of insoluble  $\text{Li}_2\text{S}_2/\text{Li}_2\text{S}$  from  $\text{Li}_2\text{S}_4$  appears to be the bottleneck, in agreement with what has been reported elsewhere,<sup>[21,45]</sup> with the large kinetic barrier hindering the sulfur reduction rate at higher currents. Figure S7, Supporting Information, shows the potential difference versus the normalized capacity of the same battery between the 0.167 and 0.558  $\text{mA g}^{-1}$  rates. The plot clearly depicts the high potential barrier region corresponding to the reduction of  $\text{Li}_2\text{S}_4$  into solid  $\text{Li}_2\text{S}_2/\text{Li}_2\text{S}$ . Therefore, overcoming these specific sluggish reaction kinetics is key to fully unlocking high-rate capability.

First-principles calculations based on density functional theory were conducted to investigate the sulfur reduction reaction (SRR) pathway on carbon surface of the CNT. The precipitation of insoluble  $\text{Li}_2\text{S}_2$  and  $\text{Li}_2\text{S}$  from  $\text{Li}_2\text{S}_4$  appears to be the rate-limiting step with high energy barrier of 0.99 and 2.04 eV than other steps (Figure 2a). This accompaniment involved the galvanostatic cycling of the lithium–sulfur cells. Furthermore, SRR were analyzed on catalyzed surface (Pt–CNT). The reduction pathways show the Pt surface lowers the energy barriers for the conversions of  $\text{Li}_2\text{S}_4 \rightarrow \text{Li}_2\text{S}$  by nearly half compared to uncatalyzed, reducing the barrier from 2.04 to 0.90 eV. Furthermore, polysulfide interaction on catalyzed and uncatalyzed surface of the CNT were examined to investigate the polysulfide anchoring. The optimized configurations of polysulfides  $\text{Li}_2\text{S}_x$  ( $x = 1, 2, 4, 6$ , and 8) and their binding with Pt-catalyzed and uncatalyzed carbon are provided in Tables S1 and S2, Supporting Information. The adsorption energies (Figure 2b) of higher order polysulfides  $\text{S}_8^{2-}$ ,  $\text{S}_6^{2-}$ , and  $\text{S}_4^{2-}$  on the Pt-anchored surface were calculated to be  $-3.3$ ,  $-3.0$ , and  $-2.8$  eV, respectively, over 2 eV stronger than on the uncatalyzed carbon ( $-0.86$ ,  $-0.72$ , and  $-0.58$  eV, for  $\text{S}_8^{2-}$ ,  $\text{S}_6^{2-}$ , and  $\text{S}_4^{2-}$ , respectively). This indicates that the Pt-catalyzed



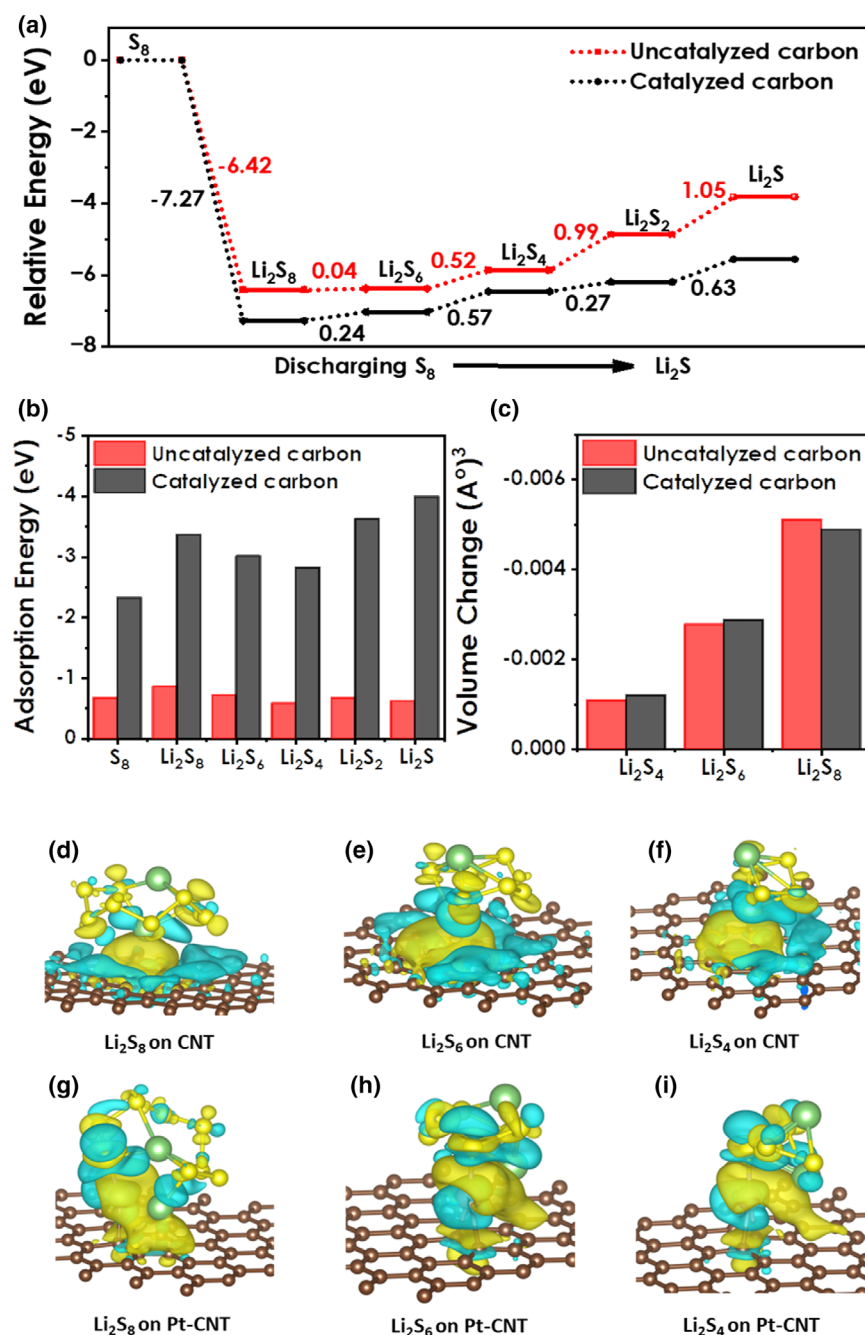


**Figure 2.** a) DFT-calculated relative energy changes of reduction of  $\text{Li}_2\text{S}_x$  ( $x=8, 6, 4, 2$ , and  $1$ ) on CNT's surface graphene layer in the presence (catalyzed) and absence (uncatalyzed) of Pt. b) Calculated adsorption energies of  $\text{S}_8$  and  $\text{Li}_2\text{S}_x$  ( $x=8, 6, 4, 2$ , and  $1$ ) in catalyzed and uncatalyzed surfaces. c) Calculated volume change of  $\text{Li}_2\text{S}_4$ ,  $\text{Li}_2\text{S}_6$ , and  $\text{Li}_2\text{S}_8$  between catalyzed and uncatalyzed surfaces. d–i) Differential charge density (DCD) calculation of  $\text{Li}_2\text{S}_4$ ,  $\text{Li}_2\text{S}_6$ , and  $\text{Li}_2\text{S}_8$  catalyzed and uncatalyzed surfaces with the yellow and cyan colors presenting charge accumulation and depletion, respectively.

carbon structure has a thermodynamically more favorable ability to adsorb polysulfides during battery operation compared to the uncatalyzed carbon.<sup>[27]</sup> The larger volume of adsorbed  $\text{Li}_2\text{S}_x$  species on the catalyst moiety compared to carbon (Figure 2c) suggests weakened effective lithium–sulfur bonds in the  $\text{Li}_2\text{S}_x$  molecules and a lower

energy barrier for their further transformation into  $\text{Li}_2\text{S}_2$  and  $\text{Li}_2\text{S}$ . Charge density difference analysis (Figure 2d–i) reveal covalent interactions between the polysulfides' S atoms and the Pt surface,<sup>[47]</sup> accounting for the higher  $\text{Li}_2\text{S}_x$  adsorption energies. This enables thermodynamically favorable precipitation and anchoring of  $\text{Li}_2\text{S}_x$  on the catalyzed surface, facilitating the discharge process. In addition, the catalyzed carbon exhibits catalytic activity for the reduction of  $\text{Li}_2\text{S}_4$  to  $\text{Li}_2\text{S}_2/\text{Li}_2\text{S}$ , identified as the potential-limiting step during lithium–sulfur battery discharge as depicted in Figure 3a–c.<sup>[21]</sup>

The theoretical calculation provides clear understanding that the catalyzed surface effectively enhances the sluggish polysulfide conversion kinetics that limit LSB performance. In support of theoretical calculations, cyclic voltammetry (CV) reveals increased redox peak currents and steeper onset slopes for the catalyzed cells compared to uncatalyzed cells scanned at the rate of  $0.01 \text{ mV s}^{-1}$  in the voltage range of  $1.7\text{--}2.8 \text{ V}$  (Figure S8, Supporting Information). The voltammograms also reveal that the most pronounced improvement was for the second reduction peak around  $2.1 \text{ V}$  representing the reduction of  $\text{Li}_2\text{S}_4$ . Meanwhile the first reduction peak at  $2.3 \text{ V}$  representing the reduction of long chain polysulfides only had minimal change as shown in Figure S8. Tafel slope as an indicator for the kinetics of sulfur reactions during cycling were calculated based on the  $\text{C}_1$ ,  $\text{C}_2$ , and  $\text{A}_1$  peaks in the CV profile by using Figure 3d,e.<sup>[22]</sup> The catalyzed cell shows the lower slope ( $\text{C}_1 = 50$ ,  $\text{C}_2 = 24$ , and  $\text{A}_1 = 47.3 \text{ mV dec}^{-1}$ ) than the uncatalyzed cell ( $\text{C}_1 = 106$ ,  $\text{C}_2 = 91$ , and  $\text{A}_1 = 70 \text{ mV dec}^{-1}$ ), indicative of accelerated kinetics during discharge and charge of the cell. Additionally, a notable decline in activation energy ( $E_a$ ) was observed via temperature-dependent CV,<sup>[25]</sup> (Figure S8) directly confirming that the impact imparted by the Pt-catalyzed carbon is in fact a catalytic effect (Figure 3e,f). Using the slope fit of the natural log of peak currents of the second reduction peak ( $2.1 \text{ V}$ ) versus  $1/T$  helped to calculate the  $E_a$  for both catalyzed and uncatalyzed cathodes (Figure 3g, h) showing a drop of the  $E_a$  for the catalyzed cell. It can be observed that at  $0.05 \text{ mV s}^{-1}$  (Figure S8) versus  $0.01 \text{ mV s}^{-1}$  (Figure 3d,e), the difference in catalytic effect between oxidation and reduction processes could be attributed

to the asymmetric nature of Li–S electrochemistry, where the multistep reduction of sulfur to  $\text{Li}_2\text{S}$  during discharge is more kinetically challenging than the reverse oxidation process. Electrochemical impedance spectra also exhibited substantially reduced (half) charge transfer resistance ( $R_{\text{CT}}$ ) at the second voltage plateau with the catalyzed ( $10 \Omega$ )

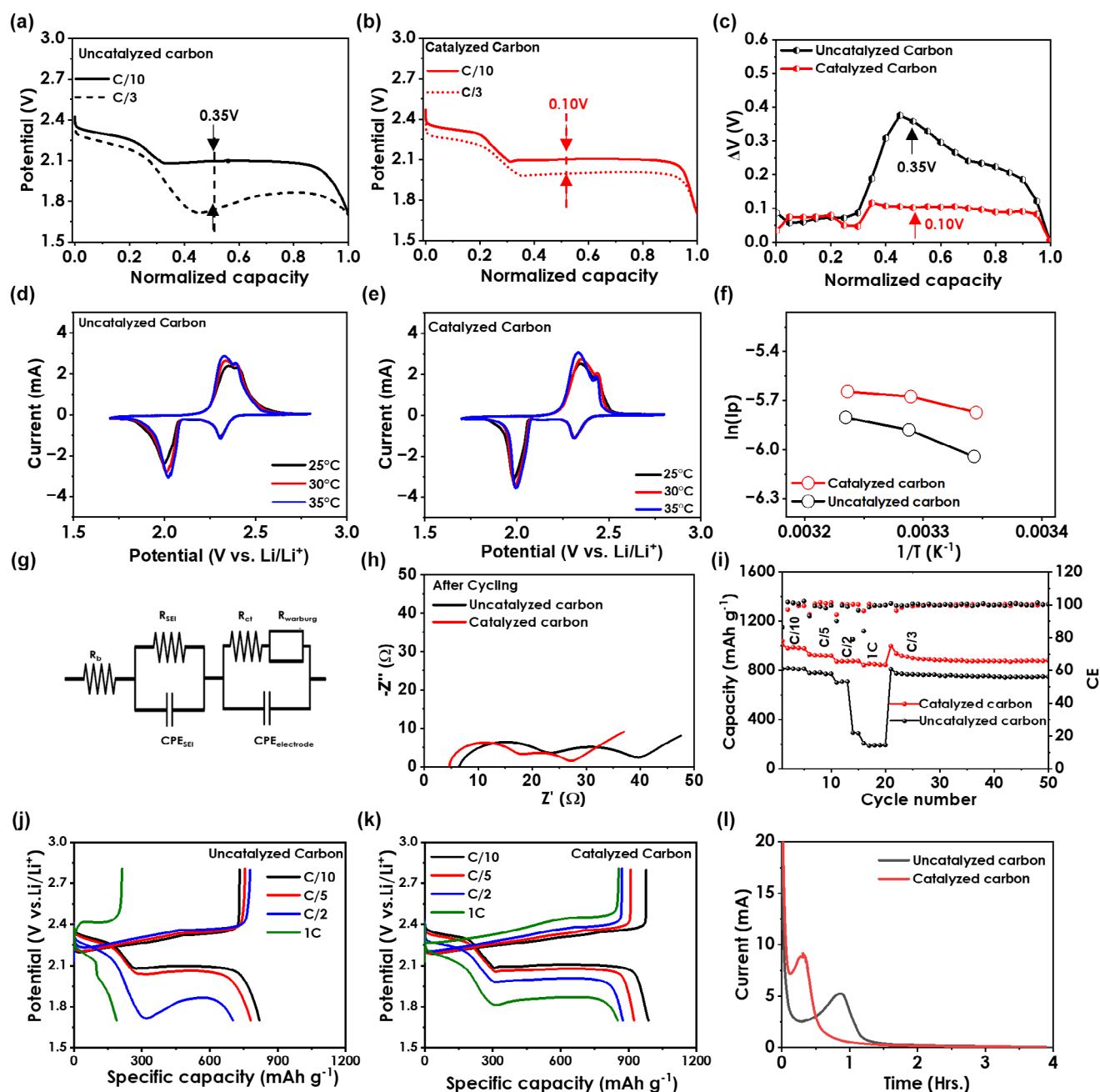


**Figure 3.** Potential versus normalized capacity of a) uncatalyzed and b) catalyzed cells comparing the cells at 0.167 and 0.558 A g<sup>-1</sup> and showing a potential barrier  $\Delta V$  of 0.35 V for uncatalyzed and 0.10 V for catalyzed. c) Comparison of the  $\Delta V$  between the 0.167 and 0.558 A g<sup>-1</sup> highlighting the potential barrier difference between the catalyzed and uncatalyzed cells. CV at different temperature of 25, 30, and 35 °C for d) uncatalyzed and e) catalyzed cells. f) Plot of natural log of peak current versus  $1/T$  of the CV at different temperatures. EIS study with g) equivalent circuit model of the Li-S cell and h) Nyquist plots comparison of catalyzed and uncatalyzed cells.<sup>[48]</sup> i) Rate capability comparison of catalyzed and uncatalyzed cells at 0.167, 0.335, 0.833, 1.675, and 0.588 A g<sup>-1</sup> rates with resulting voltage profiles for j) uncatalyzed and k) catalyzed cells. l) Potentiostatic current profile of catalyzed and uncatalyzed cells at 1.8 V.

versus uncatalyzed (19  $\Omega$ ) cathodes (Figure 3h), pinpointing kinetics as the origin of the voltage gap.

Rate capability cycling and galvanostatic charging/discharging further validates the kinetic improvement, with the large discharge overpotential present without catalyst mitigation in the catalyzed cells, especially at higher current densities (Figure 3i–k). This voltage profile

enhancement specifically corresponds to the potential-limiting precipitation reaction identified through computations. Potentiostatic measurements (Figure 3l) allow the deconvolution of the solvation and precipitation currents<sup>[49]</sup> showing comparable S<sub>8</sub> dissolution but markedly enhanced kinetics during the conversion to solid products with the catalyst. Taken together, these electrochemical diagnostics

conclusively prove that the Pt electrocatalysts alleviated the hindered reaction kinetics that constrain the battery capacity. Moreover, the solid product formation occurs earlier on the time scale in catalyzed cells (Figure 3I), suggesting faster nucleation kinetics afforded by the electrocatalysts. Quantification of the polysulfide contents at various states of discharge based on the current values provides further critical insights, as discussed in the next section.

Leveraging the potentiostatic data (Figure S9, Supporting Information), the individual dissolution and precipitation rates can be construed from the current profiles.<sup>[50]</sup> Then, using a simple, zero-dimensional, and three-reactions model (Equations 1–3), the concentrations of the different sulfides at various depth of discharge states were modeled (Supporting equations 8–14, Supporting Information).



The calculations reveal key insights into how the catalyzed carbon influences the  $Li_2S_x$  distribution. While both Pt-catalyzed and uncatalyzed cells show rapid consumption of cyclo- $S_8$  and slower depletion of  $S_8$ , maxima in  $Li_2S_4$  concentration were observed at the start of the precipitation (second voltage plateau). From these concentration plots, Pt seems to depress the peak  $Li_2S_4$  accumulation and enables its complete conversion by the full discharged state. This depressed high-order polysulfide retention aligns with XPS quantification of the discharge products, which verifies the elimination of residual  $Li_2S_4$  in catalyzed cells.<sup>[51,52]</sup> In this work,  $Li_2S$  binding energies corresponded to 160.2 eV, while  $Li_2S_2$  (terminal sulfur) corresponded to 161.8 eV as previously reported by Chu et al.<sup>[53]</sup> Furthermore, an increased  $Li_2S$  to  $Li_2S_2$  ratio is attained with catalysis, likely due to testing at higher rates ( $0.558 \text{ A g}^{-1}$ ) which exposes the kinetic problem in uncatalyzed cells. By curtailing buildup of soluble  $Li_2S_4$  and shifting speciation away from  $Li_2S_2$ , the catalyst mitigates two key problems in LSB, namely the polysulfide loss and the poor self-catalysis once insoluble species build up on the cathode surface. Suppressing the LiPS shuttle is pivotal, as diffusion of higher order soluble sulfides leads to active material loss, anode corrosion, and poor cycling efficiency.<sup>[1]</sup> Both the catalyst and the carbon surfaces demonstrate electrochemical activity initially. However, as discharge products predominantly composed of  $Li_2S_2$  and  $Li_2S$  build up, the composition of these solids can impact further conversion due to their diminished catalytic activity relative the Pt or CNT surfaces. Previous studies on electronic and ionic conductivity as well as electrocatalytic selectivity between  $Li_2S_2$  and  $Li_2S$  suggest  $Li_2S$  is the more active species in LSBs.<sup>[21,29]</sup> Preferentially depositing  $Li_2S$  over  $Li_2S_2$  early in discharge thus helps sustain an electroactive cathode and enables higher capacity, since the conversion of  $S_8$  solely to  $Li_2S_2$  possesses only half the theoretical specific capacity compared to full reduction to  $Li_2S$ .<sup>[54]</sup> The preference toward  $Li_2S$  is tied to its higher intrinsic activity – if the accumulating discharge products are composed substantially of less active  $Li_2S_2$  which passivates conductive surfaces, subsequent polysulfide conversion could be severely hindered. Therefore, understanding the nucleation and growth mechanisms of these sulfide phases and designing materials that promote  $Li_2S$  formation are critical to further enhancing lithium–sulfur cell performance.

In addition to its electrocatalytic function in accelerating conversion reactions, Pt also serves as a crucial binding site for soluble polysulfides. This interaction facilitates electron transfer while reducing diffusion of polysulfides out of the cathode region. DFT and experimental adsorption tests indicate that Pt-CNT exhibits superior polysulfide binding compared to the carbon support alone. This aligned with visual observations showing Pt-CNT cathodes suppress the typical leaching of colored species from the cell (Figure S10, Supporting Information). The dual mechanism of enabling electron transfer to the captured polysulfides while keeping them anchored to conductive sites, even at rest, is pivotal to minimizing polysulfide concentrations in the electrolyte and ensuing shuttle to the anode. Without catalyst, significantly higher quantities of solubilized polysulfides emerge from the cathode and propagate the capacity loss associated with the shuttle effect. Ultimately, the chemical affinity between Pt and polysulfides enables the adsorption critical to high-performance LSBs (Figure 4).

Coin cell testing verifies the meaningful performance enhancements afforded by catalyzed cells under prolonged cycling. With catalysts, an initial specific capacity of  $0.98 \text{ Ah g}^{-1}$  is attained, higher than the  $0.90 \text{ Ah g}^{-1}$  without catalysts. This capacity difference expanded over 500 cycles at a moderate current of  $0.558 \text{ A g}^{-1}$ , with the catalyzed cells retaining 91.9% of initial capacity versus only 75.3% retention for the uncatalyzed cells. The voltage gap at the kinetic limitation is also suppressed with catalyst, exhibiting a 32 mV lower overpotential of the potential-limiting step at 500 cycles (Figure S11, Supporting Information). Coulombic efficiency is further improved, with the catalyst enabling  $99.86 \pm 0.44\%$  average coulombic efficiency versus  $97.58 \pm 1.99\%$  without catalysts, over the 500 cycles. Furthermore, the cycling performance of catalyzed cells with high loading, specifically at  $5 \text{ mg cm}^{-2}$  (300 cycle) and  $6 \text{ mg cm}^{-2}$  (200 cycle), was evaluated under cycling rates of  $0.335 \text{ A g}^{-1}$  and  $0.1675 \text{ A g}^{-1}$ , respectively (Figure S12, Supporting Information). These metrics clearly demonstrate the effectiveness of platinum at mitigating polysulfide shuttling and side reactions that degrade cycling.

By subtracting the discharge voltage at each depth-of-discharge for the initial cycle versus subsequent cycles, the voltage change ( $\Delta V$ ) due to aging effects was quantified. These  $\Delta V$  profiles revealed a specific kinetic barrier emerging at the onset of the second plateau, corresponding to the  $Li_2S_4$  to  $Li_2S_2$ / $Li_2S$  conversion step (Figure 5b,c). Without catalysts present,  $\Delta V$  exceeded 150 mV across a wide region of 25–45% depth-of-discharge (DOD), indicating severe impedance buildup for this critical polysulfide reduction process. However, the catalyzed cathode constrained this barrier to only 25–30% DOD with  $\Delta V$  remaining below 80 mV. These catalytic effects help explain the superior cycling achieved in catalyzed cells, contrasting with rapid capacity fading without catalyst. This diagnostic again illustrates during cycling study that soluble polysulfide to solid sulfides conversion as the pivotal limiting step dictating LSB lifetimes, which cathode electrocatalysis help address and extend. Galvanostatic intermittent titration technique (GITT) was used to assess the redox kinetics of sulfur species with and without the Pt catalysts (Figure S13, Supporting Information). The catalyzed system exhibited significantly lower internal resistance at the  $Li_2S$  nucleation and  $Li_2S$  activation points compared to the uncatalyzed system, highlighting the enhanced  $Li_2S$  nucleation kinetics with the Pt nanocatalyst. Specifically, the potential difference between the rest (OCV) and galvanostatic ( $0.558 \text{ A g}^{-1}$ ) voltage was lower for the catalyzed system, indicating that the catalyst reduces polarization and facilitates the conversion of polysulfides to  $Li_2S$ .<sup>[30]</sup>

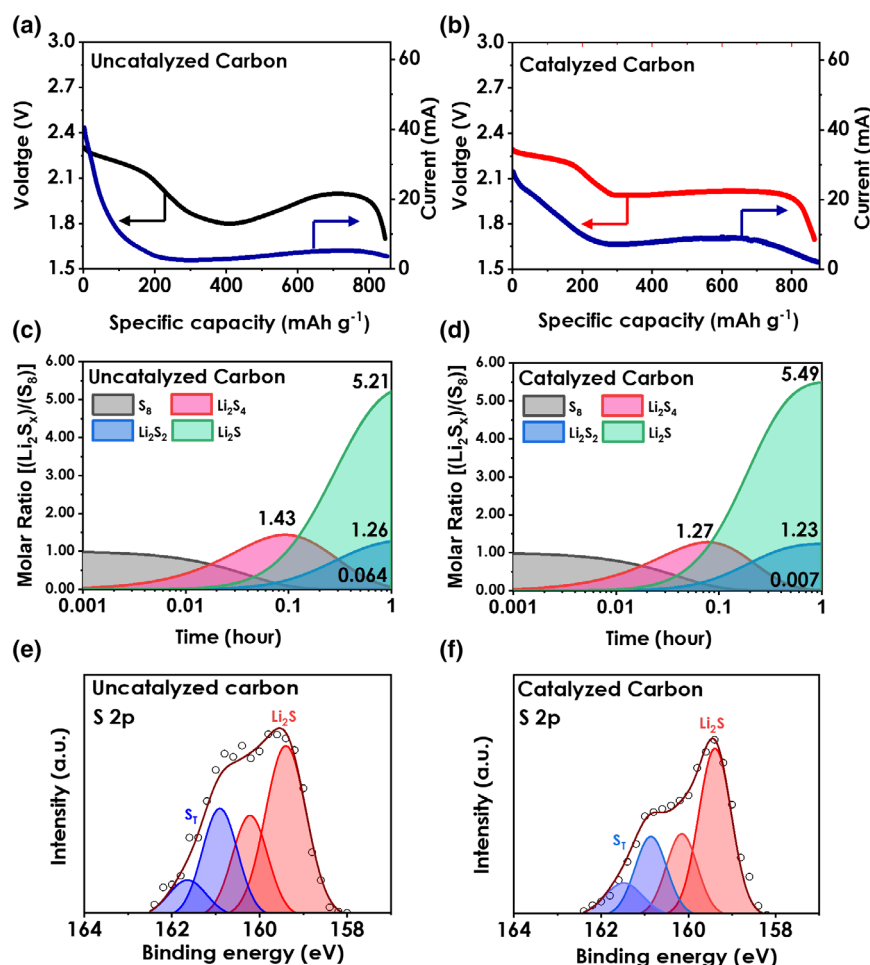


**Figure 4.** Potentiostatic (1.8 V) and galvanostatic (0.588 A g<sup>-1</sup>) profiles of a) uncatalyzed and b) catalyzed cells with the corresponding calculated active species concentrations at various specific capacities for c) uncatalyzed and d) catalyzed. XPS spectra of e) uncatalyzed and f) catalyzed cathodes after 500 cycles determining the ratios of precipitated sulfides.

Electron microscopy analyses of the fully discharged electrodes provides critical insights into the morphology using SEM (Figure S13) and localization of the sulfide discharge products facilitated preferentially by the platinum catalyst (Figure S14). Through HR-TEM coupled with selected area electron diffraction (SAED) information, the platinum nanoparticles are confirmed to remain predominantly in the Pt<sup>0</sup> metallic state after the cycling (Figure S5d,k and Figure S16).<sup>[55,56]</sup> In catalyzed cells, the discharge sulfides appear in densely clustered formations, contrasting the uniform sulfide coating in uncatalyzed cells (Figure 5e). EDS mapping reveals catalyst nanoparticles reside at the core of these sulfide aggregates (Figure 5f–i). This provides evidence for preferential polysulfide conversion at the catalyst surface, aligning with the computational predictions and was observed to be a widespread, rather than an isolated, phenomenon as shown by SEM (Figure S14, Supporting Information). Further SAED analysis (Figure 5j) indicates the sulfide clusters are primarily composed of Li<sub>2</sub>S rather than Li<sub>2</sub>S<sub>2</sub>, explaining the increased Li<sub>2</sub>S fraction observed by XPS.<sup>[53]</sup> Additionally, the crystallinity of the insoluble products formed in the presence of catalyst appears enhanced as depicted in Figure 5j and Figures S15, Supporting Information. As elucidated in previous

mechanistic work, crystalline Li<sub>2</sub>S is thermodynamically and kinetically favored over amorphous Li<sub>2</sub>S.<sup>[57]</sup> Without an electrocatalyst, the high activation barriers promote accumulation of sluggish, irregularly shaped amorphous Li<sub>2</sub>S (with no distinct SAED pattern), while electrocatalysis reduces the nucleation and growth barriers, allowing the system to preferentially form higher activity crystalline Li<sub>2</sub>S. Overall, the TEM, EDS, and SAED results supply proof that the electrocatalyst seeds the targeted deposition of discharge products suited for a long-life LSB. Furthermore, the long cycling test for the catalyzed cell was carried out at different sulfur loadings, comparable to the previous report (Table S3). The cells exhibited a capacity fade of 40% versus 51% after 1000 cycles at 2C for catalyzed and uncatalyzed, respectively (Figure 6a,f). Similarly cells had 14% versus 42% capacity loss after 500 cycles at 1C for catalyzed versus uncatalyzed, respectively (Figure 6b,g). Additionally, catalyzed cells with high sulfur loading (> 5 mg cm<sup>-2</sup>) demonstrated approximately 88% capacity retention after 300 cycles at 0.2C (5 mg cm<sup>-2</sup>) and 89% after 200 cycles at 0.1C (6 mg cm<sup>-2</sup>) as shown in Figure 6c,d. Their uncatalyzed counterparts were unable to complete the same number of cycles (Figure 6h,i) and had less than 40% capacity retention at the same loading and C-rate. A comparison of initial capacity and capacity fade rate are shown in Table S3, comparing this work to prior art. During the capacity fade study, we observed that the capacity can increase over the course of several cycles. This phenomenon likely results from the complex interplay between cycling rates, sulfur loadings, and electrochemical processes in Li–S batteries.

We hypothesize that this capacity increase stems from a gradual activation process involving improved electrolyte penetration, enhanced sulfur utilization, and stabilization of the solid electrolyte interphase (SEI) on the lithium anode. In addition, as sulfur loading increases, the cathode thickness necessarily grows, leading to a cascade of effects that impact battery performance. The thicker cathode structure impedes Li<sup>+</sup> transport, particularly to the deeper regions of the electrode, resulting in reduced sulfur utilization, especially at higher C-rates. This transport limitation creates concentration gradients within the cathode, causing uneven reaction rates and localized stress that can accelerate degradation over multiple cycles. Moreover, the increased sulfur content amplifies the formation of soluble polysulfides, which can more readily saturate the electrolyte. This saturation exacerbates the shuttle effect, where polysulfides migrate to the anode and back, leading to active material loss and reduced coulombic efficiency. The combination of these factors – hindered ion transport, uneven reaction distribution, and enhanced polysulfide shuttling – collectively contribute to the observed decline in cyclability, sulfur utilization, and coulombic efficiency as areal sulfur loading increases.

Multilayer pouch cells with 5 cm × 5 cm active area per layer (total of four layers) and with sulfur loading of 5 mg cm<sup>-2</sup> were prepared to



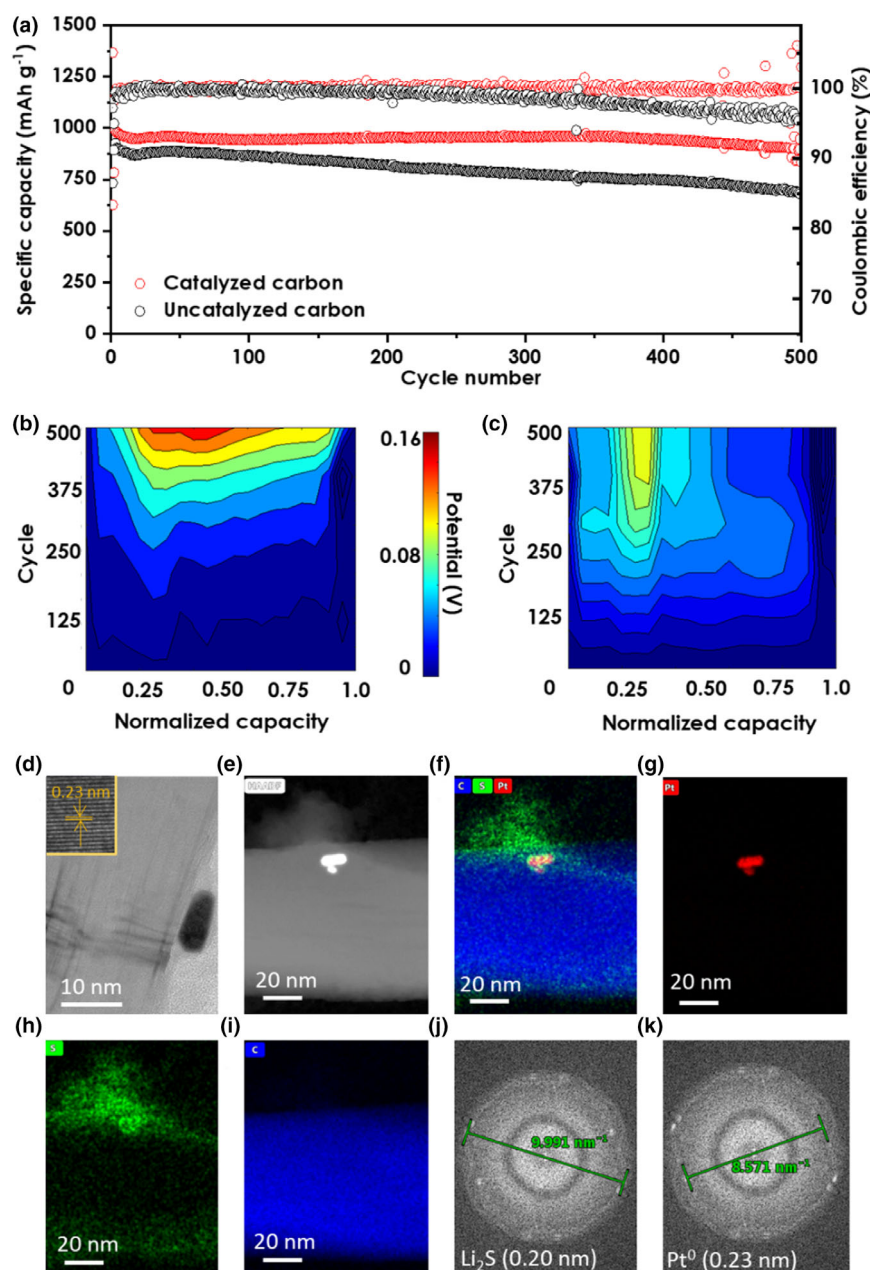


**Figure 5.** a) Charge discharge cycling performance of catalyzed versus uncatalyzed cells ( $3.4 \text{ mg cm}^{-2}$ ) showing specific capacity retention and coulombic efficiency over 500 cycles. Heat map plot of the potential change from cycles 1 to 500 compared to the initial cycle showing the major potential barrier regions for b) uncatalyzed and c) catalyzed. A close-up of a region showing Pt nanoparticle on the CNT d) HR-TEM with inset showing d-spacing of the Pt, e) HAADF, and EDX image of f) the overlaid C, S, and Pt elements, g) platinum, h) sulfur, i) carbon. SAED patterns of j) precipitation species confirming  $\text{Li}_2\text{S}$  and k) platinum nanoparticle.

test the performance at scaled up conditions. Figure 6e shows stable cell performance for the initial 15 cycles at  $0.067^\circ\text{C}$  with coulombic efficiencies exceeding 97% at mild pressure of 5 kPa. This further demonstrates the improvement afforded by the electrocatalysts and its potential to translate in commercially relevant systems.

## 4. Conclusion

In summary, platinum nanocatalysts exhibit potent electrocatalytic effects on the sluggish polysulfide conversion reactions that are most problematic under lean electrolyte conditions. Experimental (XPS, TEM) along with established semi-empirical model which verifies the elimination of residual  $\text{Li}_2\text{S}_4$  in Pt catalyzed cells and enables accelerated polysulfide conversion by the full discharged state. Further optimizing of the catalyst composition, dispersion, and loading on suitable carbon supports may enable more durable and efficient utilization of the catalyst for enhanced lithium–sulfur battery performance. By overcoming three major problems in the cell, namely passivating sulfide precipitation, sluggish kinetics, and polysulfide loss, Pt-catalyzed cells were afforded a 17% enhancement in capacity retention over 500 cycles with an average of 2.4% improvement in coulombic efficiency versus uncatalyzed cells. The catalyst elevated LSB's performance at high c-rates (2C and 1C), at high loadings ( $5\text{--}6 \text{ mg cm}^{-2}$ ), and in multilayer pouch cells presents it as a viable technology for applications requiring extended cycle life.

## 5. Experimental Section

**Materials:** Multiwalled carbon nanotubes (MWCNTs) (50–90 nm diameter >95% carbon basis), platinum (IV) nitrate where obtained from Alfa Aesar. Nitric Acid 70%, acetone (99.5%), Sulfur powder (99.98% trace metal basis), carbon black, Super P, and lithium metal foil were obtained from Sigma-Aldrich. Aluminum foil current collectors, Al (>99.5% purity), polyvinylidene fluoride binder, and (PVDF) (99.6%) were obtained from MSE Supplies. N-methyl-2-pyrrolidone (NMP) (99.5%), bis(trifluoromethylsulfonyl) imide, (LiTFSi) (>98%), 1,3-dioxolane (DOL) (99.5%), and lithium nitrate ( $\text{LiNO}_3$ ) (99.99% trace metals basis) were obtained from Thermos scientific. Solvent 1,2-dimethoxyethane (DME) (99.5%) was obtained from Spectrum Chemicals. Polypropylene separator was obtained from Celgard (2500). CR2032 coin cell casing, cap, gaskets, springs, and spacers were obtained from UMC supplies.

**Methods:** *Pt-CNT preparation*—Aqueous platinum (IV) nitrate salt solution with concentration to yield 1 wt% of Pt/CNT was first prepared in 100 mL deionized water, then added dropwise to 6 g of de-aired multiwall CNT. The resulting slurry was rested for 1 h then dried for 12 h at  $110^\circ\text{C}$ . The dried product was then oxidized at  $350^\circ\text{C}$  for 2 h under dry air flow followed by hydrogen reduction at  $500^\circ\text{C}$  for 2 h under 10% hydrogen in argon. X-ray diffraction (XRD) of the Pt-CNT before and after oxidation is shown in Figure S1c, Supporting Information.

*Sulfur–carbon composite preparation*—A melt-diffusion method was chosen. A 80:20 ratio of S/Pt-CNT was mixed with mortar and pestle and added to an



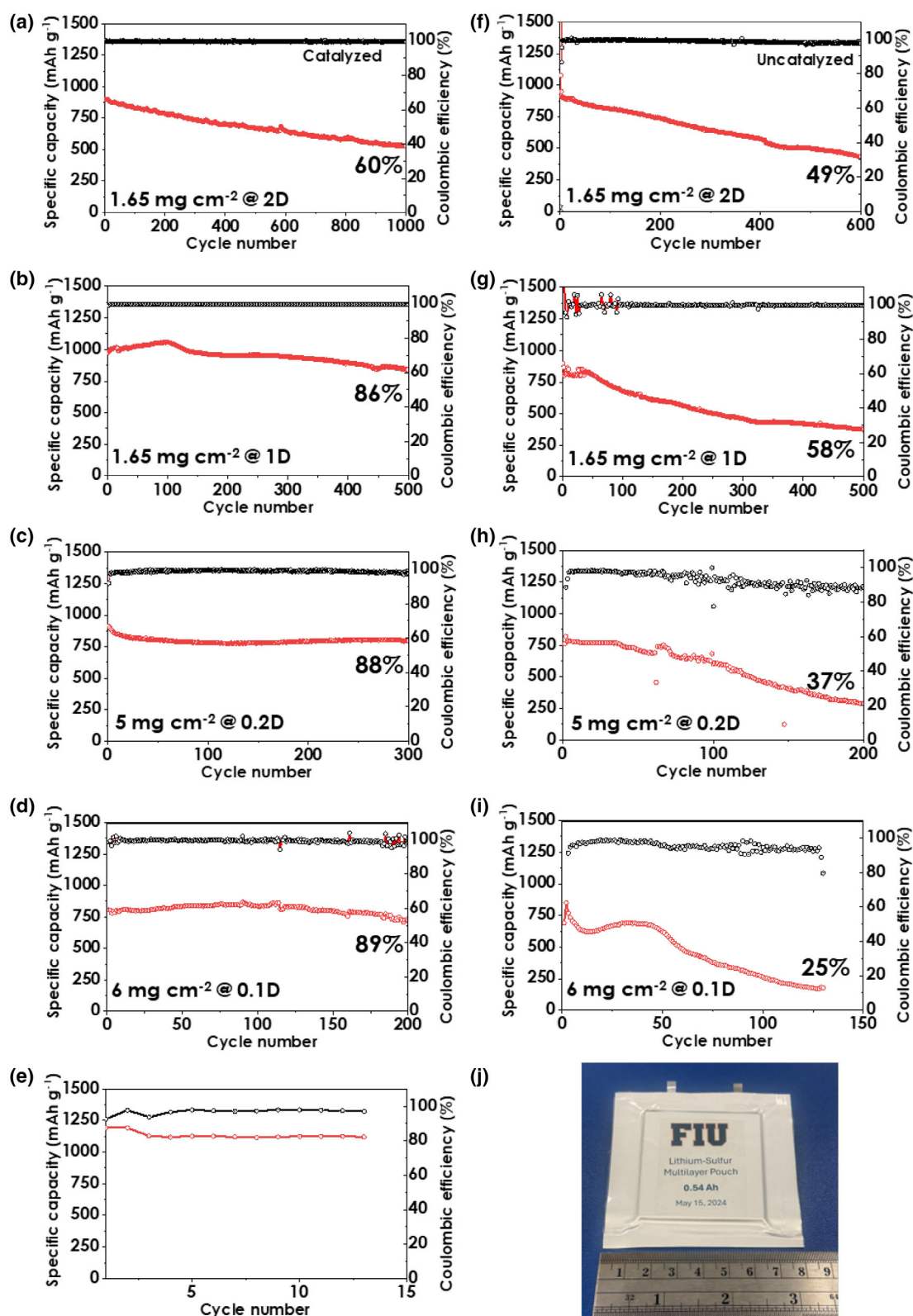


**Figure 6.** Cycling performance of catalyzed cells at a) 2C over 1000 cycles ( $1.65 \text{ mg cm}^{-2}$ ), b) 1C over 500 cycles ( $1.65 \text{ mg cm}^{-2}$ ), c) 0.2C over 300 ( $5 \text{ mg cm}^{-2}$ ), d) 0.1C over 200 cycles ( $6.0 \text{ mg cm}^{-2}$ ), and e) Pouch cell with  $5 \text{ mg cm}^{-2}$  at 0.05C with j) inset of photograph of a  $5 \text{ cm} \times 5 \text{ cm}$  multilayer pouch cell with a total of four layers and a 0.05C capacity of 0.54 Ah and Cycling performance of uncatalyzed cells f) 2C over 600 cycles ( $1.65 \text{ mg cm}^{-2}$ ), g) 1C over 500 cycles ( $1.65 \text{ mg cm}^{-2}$ ), h) 0.2C for 200 ( $5 \text{ mg cm}^{-2}$ ), i) 0.1C for 130 cycles ( $6.0 \text{ mg cm}^{-2}$ ).

autoclave jar assembled and sealed under argon. The mixture was heated to 155 °C and maintained for 16 h to get a homogeneous mixture. The resultant product was collected and stored under argon for later use in slurry preparation. X-ray photoelectron spectroscopy (XPS) and Raman spectroscopy analyses of the composite are shown in Figure S1a,b, Supporting Information.

**Cathode preparation**—Cathodes were prepared following a slurry-casting method of a mixture of 80% of the sulfur–carbon composite, 10% carbon black (Super P), 10% and PVDF binder, by weight in NMP solvent. The cathode films were dried for 12 h at 60 °C under vacuum then stored under argon for an additional 24 h. The dry films areal loading of sulfur was controlled to be about 3.0–4.0 mg cm<sup>−2</sup>. Transmission electron microscopy (TEM) of the cathode materials is shown in Figure S2, Supporting Information. The sulfur loading was confirmed using thermogravimetric analysis (TGA) which confirmed 64% by weight of sulfur in the dry cathodes (Figure S3, Supporting Information). The distribution of the Pt catalyst in the cathode is shown in top and cross-sectional views using SEM/EDS in Figure S4, Supporting Information.

An optimization study was conducted to determine the ideal Pt loading balancing performance and economic factors. The impact of Pt loading was evaluated at 1C rate, where catalytic effects are most evident. Stable cycle capacity was plotted against Pt weight percentage (Figure S5, Supporting Information).

**Coin cell preparation**—Coin cells (CR2032) were assembled under argon using 15 mm diameter cathodes, Li metal foil anode, 16 mm lithium disk, and a Celgard 2500 monolayer membrane separator. The electrolyte was prepared by dissolving 1 M LiTFSi (>99%), 0.2 M LiNO<sub>3</sub> (99.9%) in 1:1 DOL:DME (v/v) at room temperature under argon. The electrolyte to sulfur ration (E/S) ratio was maintained at 6 μL mg<sup>−1</sup> throughout this study. The assembled coin cells were rested for at least 2 h to stabilize their OCV were cyclically charged and discharged in the voltage window of 1.7–2.8 V versus Li<sup>+</sup>/Li using an Arbin, LBT20087 tester. Other electrochemical studies that used cyclic voltammetry (1.7–2.8 V under 0.01–1 mV s<sup>−1</sup>, as indicated), electrochemical impedance spectroscopy (AC 1 mV, 10 mHz–1 MHz), and chronoamperometric tests all used Gamry Interface 1010E tester.

**Pouch cell preparation**—Pouch cells with 5 cm × 5 cm active area dimensions were prepared using 5 mg cm<sup>−2</sup> of sulfur using the compositions described above. Double-sided lithium on copper (50 μm per side) was used as anode. An E/S ratio of 4 μL mg<sup>−1</sup> was used. The pouch was tested under an applied pressure of ~5 kPa and cycled at 0.067C.

## Acknowledgments

The authors acknowledge financial support from Lion Battery Technologies Inc. The computational works used Bridges-2 at Pittsburgh Supercomputing Center through allocation Discover MAT230033 from the Advanced Cyberinfrastructure Coordination Ecosystem: Services & Support (ACCESS) program, which is supported by National Science Foundation grants #2138259, #2138286, #2138307, #2137603, and #2138296. The Bridges-2 system is supported by NSF award number ACI-1928147, at the Pittsburgh Supercomputing Center (PSC). The authors acknowledge Mr. Arvind Kasbe for his help in the preparation of some of the artworks.

## Conflict of Interest

The authors declare that they have no known competing financial interests or personal relationships that could have appeared to influence the work reported in this article.

## Data Availability

Data will be made available on request.

## Supporting Information

Supporting Information is available from the Wiley Online Library or from the author.

## Keywords

batteries, catalysts, electrochemistry, electrodes, energy materials

Received: August 16, 2024

Revised: September 28, 2024

Published online: October 12, 2024

- [1] Z. X. Chen, M. Zhao, L. P. Hou, X. Q. Zhang, B. Q. Li, J. Q. Huang, *Adv. Mater.* **2022**, *34*, e2201555.
- [2] M. Y. Wang, Z. C. Bai, T. Yang, C. H. Nie, X. Xu, Y. X. Wang, J. Yang, S. X. Dou, N. N. Wang, *Adv. Energy Mater.* **2022**, *12*, 2201585.
- [3] H. J. Peng, J. Q. Huang, X. B. Cheng, Q. Zhang, *Adv. Energy Mater.* **2017**, *7*, 1700260.
- [4] A. Manthiram, S. H. Chung, C. X. Zu, *Adv. Mater.* **2015**, *27*, 1980.
- [5] Z. H. Shen, X. Jin, J. M. Tian, M. Li, Y. F. Yuan, S. Zhang, S. S. Fang, X. Fan, W. G. Xu, H. Lu, J. Lu, H. G. Zhang, *Nat. Catal.* **2022**, *5*, 555.
- [6] Y. Chen, T. Y. Wang, H. J. Tian, D. W. Su, Q. Zhang, G. X. Wang, *Adv. Mater.* **2021**, *33*, 2003666.
- [7] H. J. Peng, G. Zhang, X. Chen, Z. W. Zhang, W. T. Xu, J. Q. Huang, Q. Zhang, *Angew. Chem. Int. Edit.* **2016**, *55*, 12990.
- [8] H. Zhang, L. K. Ono, G. Q. Tong, Y. Q. Liu, Y. B. Qi, *Nat. Commun.* **2021**, *12*, 4738.
- [9] T. Liu, Z. Shi, H. J. Li, W. J. Xue, S. S. Liu, J. M. Yue, M. L. Mao, Y. S. Hu, H. Li, X. J. Huang, L. Q. Chen, L. M. Suo, *Adv. Mater.* **2021**, *33*, e2102034.
- [10] W. C. Ren, W. Ma, S. F. Zhang, B. T. Tang, *Energy Storage Mater.* **2019**, *23*, 707.
- [11] J. Zhang, C. Y. You, J. Wang, H. Xu, C. Z. Zhu, S. H. Guo, W. H. Zhang, R. Yang, Y. H. Xu, *Chem. Eng. J.* **2019**, *368*, 340.
- [12] W. D. Zhou, C. M. Wang, Q. L. Zhang, H. D. Abruña, Y. He, J. W. Wang, S. X. Mao, X. C. Xiao, *Adv. Energy Mater.* **2015**, *5*, 1401752.
- [13] S. A. Lateef, M. Manjum, H. A. Mcray, W. E. Mustain, G. Jalilvand, *ACS Appl. Energy Mater.* **2023**, *6*, 9307.
- [14] G. F. Zeng, Y. P. Liu, D. J. Chen, C. Zhen, Y. P. Han, W. D. He, *Adv. Energy Mater.* **2021**, *11*, 2102058.
- [15] F. C. Zhang, Z. H. Tang, L. R. Zheng, T. F. Zhang, M. Y. Xu, H. Xiao, H. F. Zhuang, P. Y. Han, Q. M. Gao, *Appl. Catal. B Environ.* **2023**, *334*, 122876.
- [16] H. F. Zhuang, T. F. Zhang, H. Xiao, F. C. Zhang, P. Y. Han, H. F. Gu, J. R. Jiao, W. X. Chen, Q. M. Gao, *Appl. Catal. B Environ. Energy* **2024**, *340*, 123273.
- [17] H. Chen, Z. Z. Wu, M. T. Zheng, T. C. Liu, C. Yan, J. Lu, S. Q. Zhang, *Mater. Today* **2022**, *52*, 364.
- [18] P. Wang, B. J. Xi, M. Huang, W. H. Chen, J. K. Feng, S. L. Xiong, *Adv. Energy Mater.* **2021**, *11*, 2002893.
- [19] L. Zhou, D. L. Danilov, F. Qiao, J. F. Wang, H. T. Li, R. A. Eichel, P. H. L. Notten, *Adv. Energy Mater.* **2022**, *12*, 2202094.
- [20] S. F. Ng, M. Y. L. Lau, W. J. Ong, *Adv. Mater.* **2021**, *33*, 2008654.
- [21] Y. R. Zhong, Q. Wang, S. M. Bak, S. Hwang, Y. H. Du, H. L. Wang, *J. Am. Chem. Soc.* **2023**, *145*, 7390.
- [22] W. X. Hua, H. Li, C. Pei, J. Y. Xia, Y. F. Sun, C. Zhang, W. Lv, Y. Tao, Y. Jiao, B. S. Zhang, S. Z. Qiao, Y. Wan, Q. H. Yang, *Adv. Mater.* **2021**, *33*, 2101006.
- [23] L. L. Peng, Z. Y. Wei, C. Z. Wan, J. Li, Z. Chen, D. Zhu, D. Baumann, H. T. Liu, C. S. Allen, X. Xu, A. I. Kirkland, I. Shakir, Z. Almutairi, S. Tolbert, B. Dunn, Y. Huang, P. Sautet, X. F. Duan, *Nat. Catal.* **2020**, *3*, 762.
- [24] S. Y. Wang, Z. W. Wang, F. Z. Chen, B. Peng, J. Xu, J. Z. Li, Y. H. Lv, Q. Kang, A. L. Xia, L. B. Ma, *Nano Res.* **2023**, *16*, 4438.
- [25] W. X. Hua, T. X. Shang, H. Li, Y. F. Sun, Y. Guo, J. Y. Xia, C. N. Geng, Z. H. Hu, L. K. Peng, Z. Y. Han, C. Zhang, W. Lv, Y. Wan, *Nat. Catal.* **2023**, *6*, 174.

- [26] Y. J. Qi, N. Chai, Q. H. Gu, J. N. Chen, M. Lu, X. Zhang, B. S. Zhang, *Chem. Eng. J.* **2022**, 435, 135112.
- [27] M. Z. Sun, Z. Wang, X. Li, H. B. Li, H. S. Jia, X. X. Xue, M. Jin, J. Q. Li, Y. Xie, M. Feng, *J. Mater. Chem. A* **2020**, 8, 11818.
- [28] H. Yuan, H. J. Peng, B. Q. Li, J. Xie, L. Kong, M. Zhao, X. Chen, J. Q. Huang, Q. Zhang, *Adv. Energy Mater.* **2019**, 9, 1802768.
- [29] X. Q. Zhou, J. Zhou, L. H. Sun, S. Chen, M. Y. Wang, X. D. Meng, J. Qu, C. K. Sun, Z. Z. Yu, Y. Huang, C. W. Bielawski, J. X. Geng, *ACS Appl. Energy Mater.* **2023**, 6, 11157.
- [30] W. Zhang, H. Pan, N. Han, S. H. Feng, X. Zhang, W. Guo, P. P. Tan, S. J. Xie, Z. Y. Zhou, Q. R. Ma, X. L. Guo, A. Vlad, M. Wubbenhorst, J. S. Luo, J. Fransaer, *Adv. Energy Mater.* **2023**, 13, 2301551.
- [31] C. Y. Kung, Y. P. Chiang, T. C. Chan, S. H. Chung, *J. Power Sources* **2024**, 622, 235365.
- [32] C. Y. Kung, S. H. Chung, *Mater. Horiz.* **2023**, 10, 4857.
- [33] J. P. Shang, C. Ma, C. J. Zhang, W. W. Zhang, B. G. Shen, F. H. Wang, S. Guo, S. S. Yao, *ACS Appl. Nano Mater.* **2024**, 7, 1786.
- [34] Z. J. Lin, X. Li, W. L. Huang, X. Zhu, Y. Wang, Z. Q. Shan, *ChemElectroChem* **2017**, 4, 2577.
- [35] Z. Y. Wang, B. H. Zhang, S. Liu, G. R. Li, T. Y. Yan, X. P. Gao, *Adv. Funct. Mater.* **2022**, 32, 2200893.
- [36] F. F. Han, L. W. Fan, Z. G. Zhang, X. T. Zhang, L. L. Wu, *Small* **2023**, 20, 2307950.
- [37] F. F. Han, L. W. Fan, X. Z. Ma, H. Q. Lu, L. Li, X. T. Zhang, L. L. Wu, *Energy Environ. Mater.* **2024**, 7, e12623.
- [38] G. Kresse, J. Furthmüller, *Phys. Rev. B* **1996**, 54, 11169.
- [39] J. P. Perdew, K. Burke, M. Ernzerhof, *Phys. Rev. Lett.* **1996**, 77, 3865.
- [40] J. P. Perdew, J. A. Chevary, S. H. Vosko, K. A. Jackson, M. R. Pederson, D. J. Singh, C. Fiolhais, *Phys. Rev. B* **1992**, 46, 6671.
- [41] S. Grimme, J. Antony, S. Ehrlich, H. Krieg, *J. Chem. Phys.* **2010**, 132, 154104.
- [42] H. J. Monkhorst, J. D. Pack, *Phys. Rev. B* **1976**, 13, 5188.
- [43] K. Momma, F. Izumi, *J. Appl. Crystallogr.* **2011**, 44, 1272.
- [44] M. Manadé, F. Viñes, F. Illas, *Carbon* **2015**, 95, 525.
- [45] Y. T. Liu, Y. Elias, J. S. Meng, D. Aurbach, R. Q. Zou, D. G. Xia, Q. Q. Pang, *Joule* **2021**, 5, 2323.
- [46] P. Xue, K. P. Zhu, W. B. Gong, J. Pu, X. Y. Li, C. Guo, L. Y. Wu, R. Wang, H. P. Li, J. Y. Sun, G. Hong, Q. Zhang, Y. G. Yao, *Adv. Energy Mater.* **2022**, 12, 2200308.
- [47] Z. Li, J. Zhang, B. Guan, D. Wang, L. M. Liu, X. W. Lou, *Nat. Commun.* **2016**, 7, 13065.
- [48] Y. Yang, W. X. Hu, Y. F. Peng, Y. M. Wei, *J. Phys. Chem. C* **2023**, 127, 4465.
- [49] F. Y. Fan, W. C. Carter, Y. M. Chiang, *Adv. Mater.* **2015**, 27, 5203.
- [50] U. Gulzar, A. Loneragan, V. Egorov, Y. Zhang, A. Grant, A. Carroll, C. O'Dwyer, *J. Electrochem. Soc.* **2023**, 170, 030503.
- [51] W. Guo, W. Y. Zhang, Y. B. Si, D. H. Wang, Y. Z. Fu, A. Manthiram, *Nat. Commun.* **2021**, 12, 3031.
- [52] H. Sul, A. Bhargava, A. Manthiram, *Adv. Energy Mater.* **2022**, 12, 2200680.
- [53] H. Chu, H. Noh, Y. J. Kim, S. Yuk, J. H. Lee, J. Lee, H. Kwack, Y. Kim, D. K. Yang, H. T. Kim, *Nat. Commun.* **2019**, 10, 188.
- [54] J. M. Sun, Y. H. Liu, L. Liu, J. X. Bi, S. Y. Wang, Z. Z. Du, H. F. Du, K. Wang, W. Ai, W. Huang, *Adv. Mater.* **2023**, 35, 2211168.
- [55] N. Logeshwaran, I. R. Panneerselvam, S. Ramakrishnan, R. S. Kumar, A. R. Kim, Y. Wang, D. J. Yoo, *Adv. Sci.* **2022**, 9, 2105344.
- [56] T. Gan, J. X. Yang, D. Morris, X. F. Chu, P. Zhang, W. X. Zhang, Y. C. Zou, W. F. Yan, S. H. Wei, G. Liu, *Nat. Commun.* **2021**, 12, 2741.
- [57] Y. W. Song, J. L. Qin, C. X. Zhao, M. Zhao, L. P. Hou, Y. Q. Peng, H. J. Peng, B. Q. Li, *J. Energy Chem.* **2022**, 64, 568.